PHYSICAL REVIEW FLUIDS **7**, 044703 (2022)

Experimental investigation on the impingement of synthetic jet vortex rings on a spherical wall

Changlong Chen, Donglai Gao, and Wen-Li Chen*

Key Laboratory of Smart Prevention and Mitigation of Civil Engineering Disasters of the Ministry of Industry and Information Technology, Harbin Institute of Technology, Harbin 150090, China and Key Laboratory of Structures Dynamic Behavior and Control of the Ministry of Education, Harbin Institute of Technology, Harbin 150090, China

(Received 24 January 2022; accepted 31 March 2022; published 18 April 2022)

An experimental study was conducted to investigate the influence of sphere diameter and Reynolds number on synthetic jet vortex rings impinging on a spherical wall. Laser-induced fluorescence and two-dimensional particle image velocimetry techniques were applied to visualize flow and measure flow velocity, respectively. In this experiment, the stroke length was kept constant ($L = 3.6$), and different diameters ($d/D = 1$, 6, and 16) and Reynolds numbers ($\mathrm{Re}_{sj} = 227$ and 682) were analyzed. In addition to flow visualization images and phase-averaged λ_{ci} fields, the vortex ring trajectories and circulation are presented to reveal the evolution features of the vortex rings. The results demonstrated that the Reynolds number mainly determined the strength and induced ability of the primary vortex ring (PVR) and the sphere-diameter effect was reflected by the expansion distance of the PVR and its separation from the wall boundary layer. It was found that only a secondary vortex ring (SVR) was induced in the case of a small diameter or a low Reynolds number. As the diameter and Reynolds number increased, the PVR expanded continuously along the wall and induced a SVR and tertiary vortex ring. In particular, driven by the curve, the strength of the induced vortex ring decreased with the increase in the sphere diameter.

DOI: 10.1103/PhysRevFluids.7.044703

I. INTRODUCTION

The interaction of a vortex ring colliding on a wall is a significant problem that widely exists in natural phenomena and engineering practices, such as the vortex ring formed by a helicopter propeller's interaction with the fuselage or the vortex ring structure generated by the wing impacting the ground. As a basic phenomenon in fluid mechanics, the vortex ring-wall interactions have rich fluid dynamists and are an important research subject for understanding vortex dynamics.

As a typical example of a vortex ring-wall interaction, flow scenarios including the expanding of a vortex ring radius, a boundary layer with reverse vorticity, the induction of a secondary vortex ring (SVR), a tertiary vortex ring (TVR), and the rebound of a vortex ring from the wall are observed when the vortex ring approaches and orthogonally impinges on a planar wall [1]. Lim *et al.* [2] and McKeown *et al.* [3,4] conducted an experiment in which two identical vortex rings collided head on, which could simulate a free-slip wall. The vortex cores broke down into a fine-scale turbulent cloud and formed small-scale flow structures. Therefore, Lim *et al.* [2] showed that the boundary layer separation and generation of a SVR was due to the nonslip wall. Orlandi and Verzicco [5] and Swearingen *et al.* [6] numerically investigated the stability of a vortex ring during an impact event and revealed that the SVR resisted azimuthal perturbation more weakly due to vortex stretching and

---

[*] Corresponding author: cwl_80@hit.edu.cn

strain-field tilting caused by the primary vortex ring (PVR). During the impingement process, vortex ring impact, and boundary layer flow produced pushing and suction forces, respectively, which nullified each other, making the net force on the wall almost zero [7]. Naguib and Koochesfahani [8] and Cheng *et al.* [9] demonstrated that the negative-pressure sources were induced by the vortex core, whereas the positive pressure was generated by high strain rates, which were associated with the vortex near the wall and boundary layer formation. Cheng *et al.* [9] simulated an oblique collision of a vortex ring on a planar wall by the lattice Boltzmann method and found that with the decrease in the inclination angle, the vortex ring, and wall interaction induced SVRs and TVRs. Meanwhile, a helical structure was observed, which also existed in experiments [10,11].

Vortex rings impacting other wall types have also been explored, such as a cylinder [12], permeable wall [13–15], sphere [16–19], and a wall with a coaxial aperture [20]. Allen *et al.* [16] experimentally studied vortex rings colliding coaxially with a moving sphere of a small diameter. Different from a planar wall, the vortex ring passed through the sphere after the SVR was induced. Nguyen *et al.* [19] employed the vortex in cell method to numerically explore the behavior of a vortex ring when it impinged on a spherical surface with a large diameter. In axisymmetric collisions, the behavior of the PVR and SVR was dominated by two transverse components, whereas in noncoaxial collisions, the vortex-wall interaction was three dimensional, forming a complex secondary vortex structure.

A synthetic jet is vortex rings or vortex pairs produced by the periodic suction and ejection of fluid in a cavity due to the sinusoidal vibration of a diaphragm or piston. Recently, a synthetic jet as an active control strategy has attracted the interest of many researchers because it can transfer momentum without an external fluid. Moreover, due to the vortex rings produced by synthetic jets having a strong capacity to enhance flow mixing and entrainment, they have potential applications in heat transfer, such as cooling electronic components. Pavlova and Amitay [21] studied the parameters influencing the heat transfer of synthetic jets, showing that they have better heat transfer performance compared with continuous jets because of the generation of a coherent structure near the wall. Krishnan and Mohseni [22] experimentally investigated the characteristic of a wall jet induced by a circular-orifice synthetic jet impinging on a flat surface. They found that the dimensionless mean and root-mean-square velocity profiles of the wall jet showed a self-similar behavior. Furthermore, they used an empirical model to describe the velocity profiles, which can accommodate the transitional and unsteady nature of the synthetic wall jet. Xu and Wang [23], Xu *et al.* [24], and Xu and Wang [25] experimentally explored the influence of several parameters on the synthetic jet vortex ring evolution and time-mean characteristics of wall jets, including the orifice-to-wall distance, the Reynolds number, and dimensionless stroke length. They discovered that the formation of the SVR in the first few cycles was different than that in the rest of the jet cycles when the vortex rings periodically collided with the wall. When the orifice-to-wall distance was less than the stroke length, the PVR had high strength near the wall, which induced the SVR. In addition, as the Reynolds number increased, the SVR could not be induced as the PVRs quickly lost coherence. When the stroke length was large, the SVRs were stronger and formed a vortex dipole with impinging vortex rings. Xu and co-workers [26,27] and Li and co-workers [28,29] further studied synthetic jet vortex rings impinging onto a porous wall. They observed that a transmitted vortex ring was formed on the downstream side of a wall with a small hole due to vorticity cancellation, whereas a wall with a large hole could effectively achieve a downstream flow field of good quality.

Compared with a single vortex ring, consecutive vortex rings formed by a synthetic jet are more conducive to engineering applications, such as heat transfer and mixing. However, researchers have paid little attention to consecutive vortex rings impinging on curved surfaces until now. Therefore, herein, synthetic jet vortex rings impinging on a spherical wall as a typical curve surface are investigated to reveal the complex flow behavior in the impingement process. In particular, we explore the influences of Reynolds number and spherical diameter on the impingement process. In the following analysis, the experimental setting and configuration of a synthetic jet actuator are

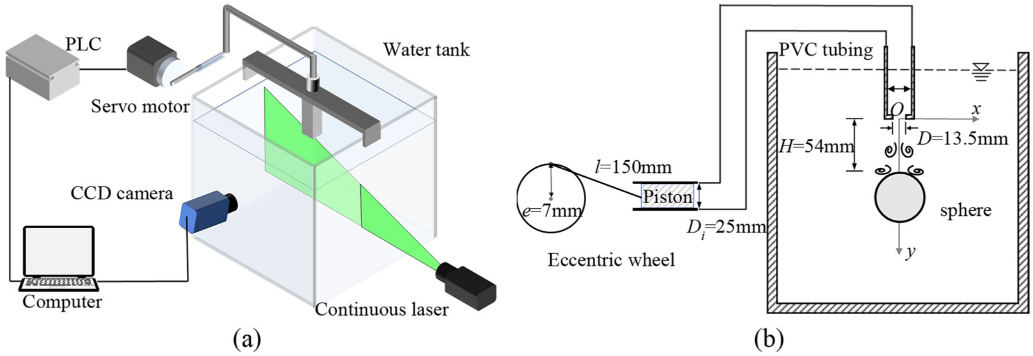

(a) (b)

FIG. 1. (a) Three-dimensional schematic of experimental setup and (b) side view of the configuration of the experimental setup.

introduced in Sec. II and flow visualization and particle image velocimetry (PIV) measurement results are presented in Sec. III. Finally, Sec. IV presents our conclusions.

II. EXPERIMENTAL DETAILS

A. Experimental setup

The current experiment was performed in a cubical water tank composed of 20-mm-thick plexiglass plates; it had a design similar to that designed in Ref. [26] (Fig. 1). The plexiglass tank size was $600\times600\times600\,\mathrm{mm}^3$, and it was large enough to avoid disturbances in the ambient fluid and ensure a quiescent flow environment for an impinging synthetic jet. To generate synthetic jet vortex rings, a hollow square cylinder with a circular orifice was placed at the center of the tank and connected to a synthetic jet actuator by PVC tubing. The diameter D of the circular orifice was 13.5 mm, and the PVC tubing inner diameter D_i was 25 mm. The synthetic jet actuator was composed of a servo motor, eccentric wheel, connecting rod, and piston-cylinder arrangement. Under the action of the connecting rod, the cyclic motion of the eccentric wheel caused the reciprocating motion of the piston, which periodically forced and sucked the fluid in the cavity through the circular orifice, forming vortex rings to convect downstream. In this actuator, the eccentric distance of the eccentric wheel was $e = 7\,\mathrm{mm}$, and the length of the connecting rod was $l = 150$ mm. Because e was much smaller than l, the piston motion can be considered sinusoidal. The instantaneous velocity $v(t)$ at the orifice center can be calculated as follows:

$$v(t) = 2\pi e f_0 \left(\frac{D_i}{D}\right)^2 \sin(2\pi f_0 t), \tag{1}$$

where f_0 is the synthetic jet excitation frequency. According to Ref. [30], the characteristic velocity of the synthetic jet U_0, defined as the time-averaged blowing velocity over the entire cycle, was expressed as

$$U_0 = \frac{1}{T}\int_0^{T/2} v(t)dt = 2ef_0\left(\frac{D_i}{D}\right)^2, \tag{2}$$

where $T = 1/f_0$ is the excitation period. In addition, the two important parameters for the synthetic jet, the dimensionless stroke length (L) and Reynolds number (Re_{sj}), can be calculated as

$$L = \frac{U_0 T}{D} = 2e\frac{D_i^2}{D^3}, \tag{3}$$

$$\mathrm{Re}_{sj} = \frac{U_0 D}{\nu} = \frac{2ef_0 D_i^2}{\nu D}, \tag{4}$$

TABLE I. Parameters for all experimental cases.

Synthetic jet parameters					Spherical wall parameters	
f_0	L	D (mm)	H (mm)	Re_{sj}	d (mm)	d/D
					13.5	1
0.4				227		
	3.6	13.5	54		81	6
1.2				682		
					216	16

where ν is the water kinematic viscosity. In the current experiment, the water temperature was approximately 15 °C and the corresponding $\nu = 1.14\times10^{-6}\,\mathrm{m}^2\,\mathrm{s}^{-1}$. For this paper, the dimensionless stroke length and distance from the orifice to the spherical vertex were kept constant at $L = 3.6$ and $H = 54$ mm, respectively. The experimental parameters for all tested synthetic jet vortex ring impingements on spherical walls are illustrated in Table I.

B. Data acquisition

In this paper, PIV and laser-induced fluorescence (LIF) techniques were applied to measure the fluid velocity field and visualize the flow structure, respectively. In the PIV experiment, hollow glass beads with an average diameter of 10 μm and a density of $1.03\,\mathrm{g/cm}^3$ were seeded into water, and their densities were close to the density of water ($1.00\,\mathrm{g/cm}^3$) so they could accurately follow the flow. A continuous laser with an output power of 5 W and a wavelength of 532 nm was used to produce an approximately 1-mm-thin laser sheet and illuminate the seeding particles on the target plane of the PIV experiment [Fig. 1(a)]. The target plane was defined as the x-y coordinate plane. The coordinate origin was chosen as the center of the circular orifice with the x axis along the circular orifice radial direction and the y axis pointing toward the jet exit [Fig. 1(b)]. A high-speed CCD camera (PCO: pco.dimax HS4, Germany) with a Sigma lens (24–70 mm F2.8 DG) was used to record the particle images, and the resolution of the camera was set at 1400×1400 pixels or larger with a corresponding field of-view of approximately $86\times86\,\mathrm{mm}^2$ ($6.3\times6.3\,D^2$). The direction of the camera lens was positioned perpendicularly to the measured plane. In the present experiment, the sample frequency was 200 and 600 Hz for $\mathrm{Re}_{sj} = 227$ and 682, respectively. The exposure time did not exceed 1 ms to ensure that particles can represent the real flow. For each case, more than 12 000 frames were captured to analyze the vortex ring evolution. The velocity fields were calculated through a multipass interrogation algorithm with an interrogation window size of 24×24 pixels and an overlap of 50%. It is important to note that the camera started capturing after, at least, 20 cycles to avoid differences between different jet cycles during impingement. In the LIF experiment, the camera position and laser sheet were the same as those during PIV, and fluorescein sodium was used as the fluorescent dye. The light source was a 100-mW, 488-nm wavelength continuous laser, and a Sony AX60 was employed to record the videos of the vortex ring evolution at 25 fps at a resolution of 3840×2160 pixels.

C. Data analysis of the PIV vector field

The azimuthal vorticity ω can be obtained by Eq. (5) using a second-order central different scheme, where u and v represent the velocity components in the x and y directions, respectively,

$$\omega = \frac{\partial v}{\partial y} - \frac{\partial u}{\partial x}. \tag{5}$$

The vortex structures were identified using the λ_{ci} method proposed by Zhou *et al.* [31], which can effectively distinguish between vortices and shear motion [32]. The definition of λ_{ci} is related to the imaginary term of the eigenvalue of the velocity gradient tensor. For a two-dimensional flow, the velocity gradient tensor D_2 was calculated as follows:

$$D_2 = \begin{bmatrix} \frac{\partial u}{\partial x} & \frac{\partial u}{\partial y} \\ \frac{\partial v}{\partial x} & \frac{\partial v}{\partial y} \end{bmatrix}. \tag{6}$$

When D_2 has a pair of complex conjugate eigenvalues $\lambda_{cr} \pm \lambda_{ci} i$ and its corresponding eigenvector $v_{cr} \pm v_{ci} i$, it can be decomposed as Eq. (7), and vortices are identified by λ_{ci}. In this paper, we determine the positive and negative $\lambda_{ci}{}'$s by vorticity to determine the vortex direction,

$$D_2 = [v_{cr} \quad v_{ci}] \begin{bmatrix} \lambda_{cr} & \lambda_{ci} \\ -\lambda_{ci} & \lambda_{cr} \end{bmatrix} [v_{cr} \quad v_{ci}]^{-1}. \tag{7}$$

Furthermore, in this paper, 3% of the λ_{ci} maximum in the flow field was selected as a threshold to determine the vortex core boundary and eliminate the background noise. The vortex circulation and vortex ring center were computed with the following equations:

$$\Gamma = \int_S \omega \, ds, \tag{8}$$

$$x_c = \frac{1}{\Gamma} \int_S x\omega \, ds, \quad y_c = \frac{1}{\Gamma} \int_S y\omega \, ds, \tag{9}$$

where Γ is the vortex circulation, x_c and y_c are the coordinates of the vortex center, and S is the area of the vortex structure determined by λ_{ci}. The vortex circulation and center position were calculated based on the phase-averaged velocity in the current paper. The phase-averaged calculation method is similar to the technique improved upon in Ref. [33]. To track the vortex rings motion, the vortex ring-type A was classified by density-based spatial clustering of applications with noise (DBSCAN) cluster analysis [34,35],

$$\{A_1, \ldots, A_k\} = \mathrm{DBSCAN}(Minpts, [r_1, r_2, r_3], [\varepsilon_1, \varepsilon_2, \varepsilon_3]), \tag{10}$$

where k is the number of different vortex rings, $Minpts$ is the number of core points, r_1, r_2, and r_3 are the distances between sample points p and q, and ε_1, ε_2, and ε_3 are the threshold corresponding to r_1, r_2, and r_3. In the current paper, r_1, r_2, and r_3 are defined as Eq. (11) and ε_1, ε_2, and ε_3 select to 0.3, 0.3, and 20,

$$r_1 = \frac{\sqrt{(x_{cp} - x_{cq})^2 + (y_{cp} - y_{cq})^2}}{D}, \quad r_2 = \left| \frac{\Gamma_p - \Gamma_q}{\Gamma_p} \right|, \quad r_3 = |t_p - t_q|. \tag{11}$$

III. RESULTS AND DISCUSSIONS

A. Evolution of vortex structures

Figure 2 shows the flow visualization images of a cycle of the synthetic jet vortex ring impinging on a $d/D = 1$ sphere surface based on LIF measurements. As mentioned in Fig. 2 and throughout the paper, $t/T = 0$ represents the moment of the beginning of the blowing stroke, whereas $t/T = 1$ is the end of the suck stroke in a jet cycle. Importantly, the flow images for vortex ring evolution were selected after eliminating the differences between different cycles. Although the dye of the first few cycles caused a disturbance in the visualization images, the main vortex structure and features were still distinguishable. Furthermore, due to the laser sheet being sheltered by the sphere model, only the left half of the flow field results was shown in the current paper. It is observed in Fig. 2

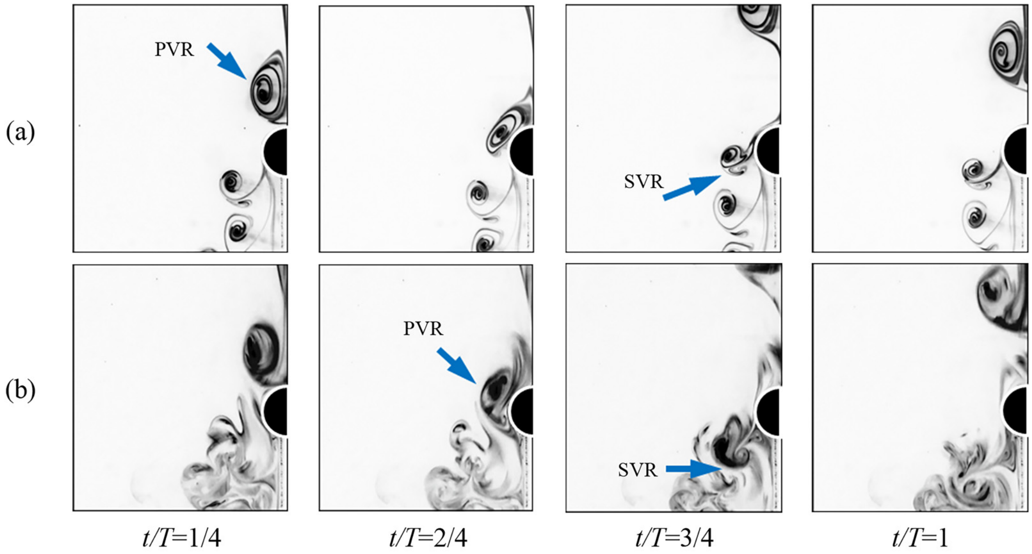

FIG. 2. Flow images of synthetic jet vortex rings impingement on a $d/D = 1$ sphere surface. (a) $\mathrm{Re}_{sj} = 227$ and (b) $\mathrm{Re}_{sj} = 682$.

that a thin fluorescent dye stripe formed when the synthetic jet vortex ring convected downstream. Gharib *et al.* [36] and Zhong *et al.* [37] indicated the trailing jet was formed when the stroke number (L) exceeded approximately 4. In the current experiment, $L = 3.6$ is smaller than the critical value of trailing jet formation. Therefore, we think the dye stripe was similar to that in Ref. [12], which was different from the trailing jet and had no influence on the impingement process.

For $\mathrm{Re}_{sj} = 227$, when the PVR impinged on the spherical surface, the vortex core became flat. Thereafter, the diameter of the primary vortex core decreased with the PVR expansion along the spherical surface. Simultaneously, the wall boundary layer was induced and separated from the spherical surface to generate the SVR due to the effect of the adverse pressure gradient. Subsequently, the SVR spread radially outward with the PVR and finally separated from the wall. The separated vortex rings convected further downstream in the streamwise direction. Eventually, the PVR and SVR diffused gradually under the influence of fluid viscosity. As observed in Fig. 2(a), the fluorescent dye can clearly describe the vortex ring structure, which indicated that the flow was laminar. The visualization images at $\mathrm{Re}_{sj} = 682$ are presented in Fig. 2(b). Similarly, a SVR with a large diameter was induced and convected downstream with the PVR during the interaction between the vortex ring and wall in this case. However, the vortex structure exhibited by LIF was fuzzy, and the vortex rings diffused rapidly after separating from the wall and transitioned to turbulence. This was because the PVR at a high Reynolds number can interact strongly with the wall, which can induce vortex rings with a high circulation and make them easier to lose coherence.

As the sphere diameter increased to $d/D = 6$ (Fig. 3), the evolution behavior was similar to its $d/D = 1$ counterpart as mentioned in the initial stages of the impingement process, such as the flow of the wall boundary layer and the stretching of the PVR along the wall. However, the subsequent flow phenomenon is quite different from that of small-diameter spheres. Obviously, for a large-diameter sphere, the primary and the induced vortex ring cannot convect downstream along the jet centerline but move on the upper surface of the sphere. Figure 3(a) shows the impingement process of a synthetic jet vortex ring at $\mathrm{Re}_{sj} = 227$. The SVR diameter was smaller than that of the case for $d/D = 1$. Additionally, it can be observed that the vortex rings formed a large-scale cluster structure after separating from the wall. Reference [23] reported a similar structure in an experiment of synthetic jet impingement onto a wall and attributed the phenomenon to a mechanism named

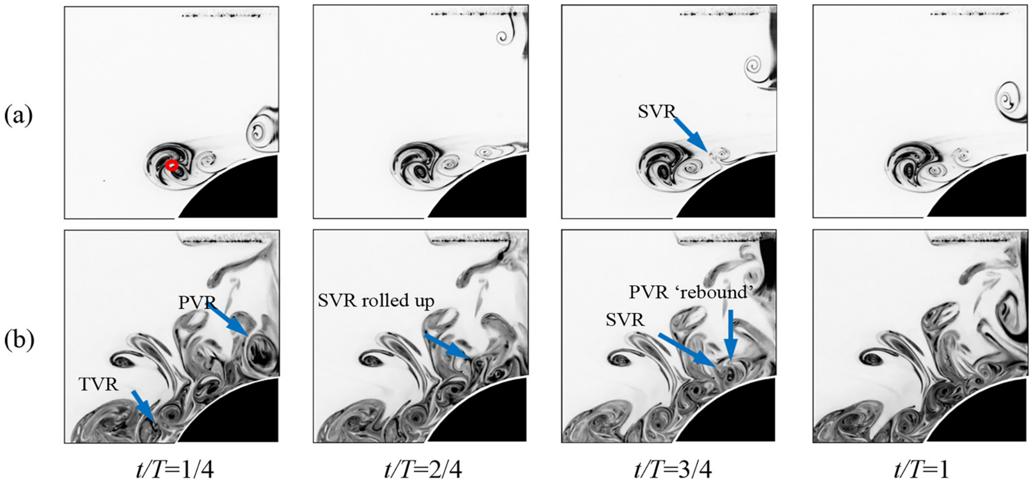

FIG. 3. Flow images of synthetic jet vortex rings impingement on a $d/D = 6$ sphere surface. (a) $\mathrm{Re}_{sj} = 227$ and (b) $\mathrm{Re}_{sj} = 682$.

"inflectional instability." However, in the current paper, we think that the formation of the cluster structure was because the vortex ring flow was laminar at a low Reynolds number. After the vortex rings dissipated under the influence of fluid viscosity, the fluorescent dyes maintained their spiral shape. As the PVR approached the wall, the previous dyes of the impinged vortex rings were pushed away and clustered with each other. Meanwhile, the cluster structure rotated around the position of the red circle marked in Fig. 3(a). With the increase in synthetic jets cycles, the structure gradually moved away from the jet centerline, which could be caused by vortex rings separating from the spherical wall. As for $\mathrm{Re}_{sj} = 682$, the behaviors of the vortex ring impingement on the wall were more complex. It can be observed that the SVR was rolled up by the PVR. Moreover, a SVR with high strength induced the rebounding of the PVR at $t/T = 3/4$. Then, the SVR was entrained into the PVR, whereas the TVR was induced due to the expansion of the PVR.

Finally, the sphere diameter was further increased to $d/D = 16$ with the impingement flow presented in Fig. 4. The shape and motion of the cluster structure were almost consistent with that in Ref. [23]. This result indicated that the vortex ring behavior of impingement onto a sphere at a low Reynolds number was similar to that of a planar wall with the increase in the sphere diameter. For $\mathrm{Re}_{sj} = 682$, the impingement process was the same as that of $d/D = 6$. When the PVR approached the wall, it induced a SVR, and, subsequently, the SVR rolled up into the PVR. Eventually, the PVR continued to expand along the wall and induced the formation of a TVR.

LIF images could show many dissipated vortex structures in previous cycles because there are many residual dyes in the flow field. Therefore, the phase-averaged λ_{ci} fields calculated from the PIV measurements for all tested cases are illustrated in Figs. 5–7 to complement the flow visualizations by LIF. Apparently, the motion of vortex structures presented by λ_{ci} was extremely consistent with that depicted in the flow visualization images, which indicated that the LIF results can describe the flow accurately.

Figure 5 clearly shows that as the PVR approached the wall at a low Reynolds number, it induced a reverse SVR, which expanded along the wall with the PVR. Finally, the PVR and SVR separated from the wall and convected downstream. Whereas at a high Reynolds number, the SVR was induced with high strength, and the vortex rings broke down downstream and transitioned to turbulence. Correspondingly, in Figs. 6 and 7, it was obvious that the PVR expanded along the spherical surface and induced a TVR at a high Reynolds number for large-diameter spheres.

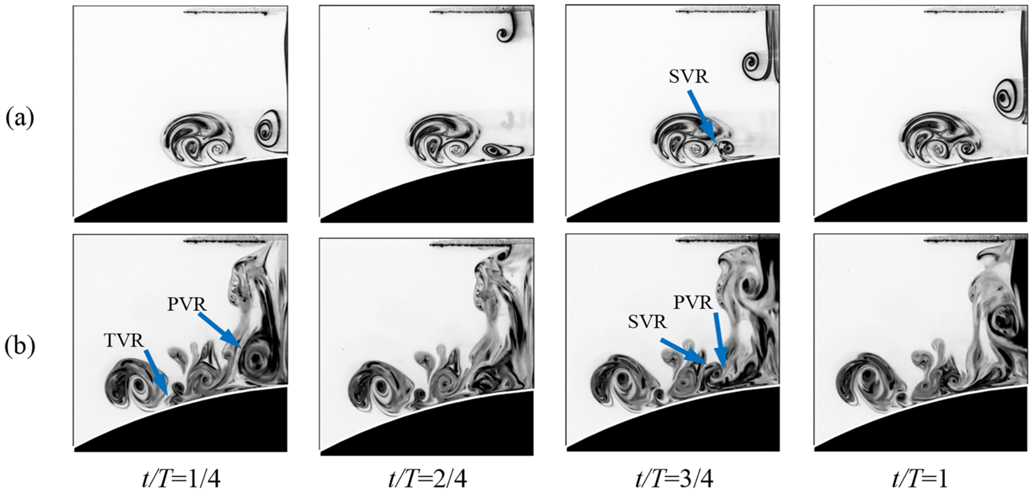

FIG. 4. Flow images of synthetic jet vortex rings impingement on a $d/D = 16$ sphere surface. (a) $\mathrm{Re}_{sj} = 227$ and (b) $\mathrm{Re}_{sj} = 682$.

Meanwhile, the expansion distance of the PVR at a high Reynolds number is longer than that at a low Reynolds number.

Comparing Figs. 5–7, we noted that λ_{ci} and of the SVR and TVR decreased gradually with the increase in the spherical diameter. In particular, the λ_{ci} of the TVR was almost zero for $d/D = 16$ at $\mathrm{Re}_{sj} = 682$. This phenomenon showed that the strength of the SVR was high for a small-diameter sphere.

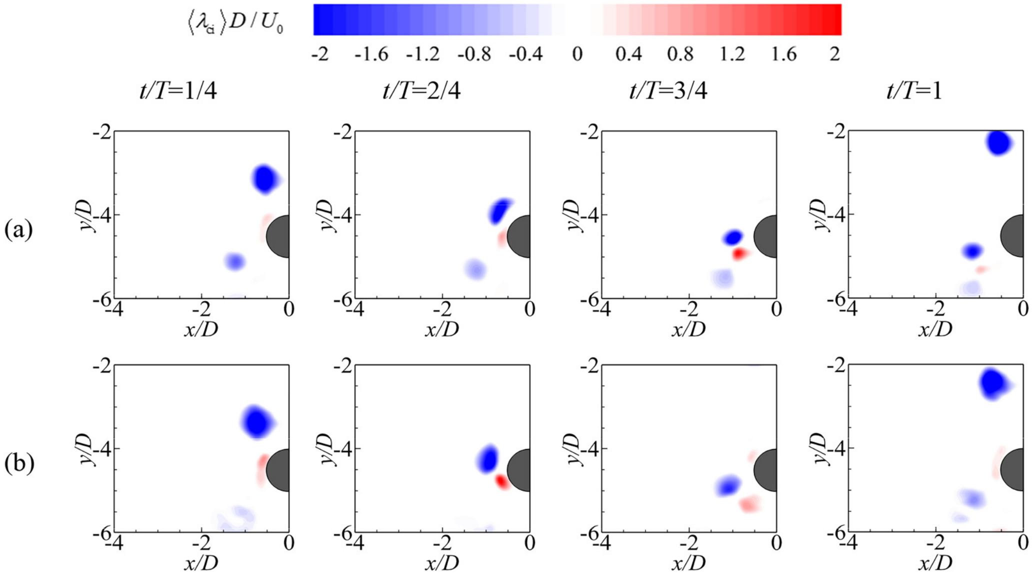

FIG. 5. Phase-averaged λ_{ci} fields of vortex ring impingement on a $d/D = 1$ sphere surface for all Reynolds numbers. (a) $\mathrm{Re}_{sj} = 227$ and (b) $\mathrm{Re}_{sj} = 682$.

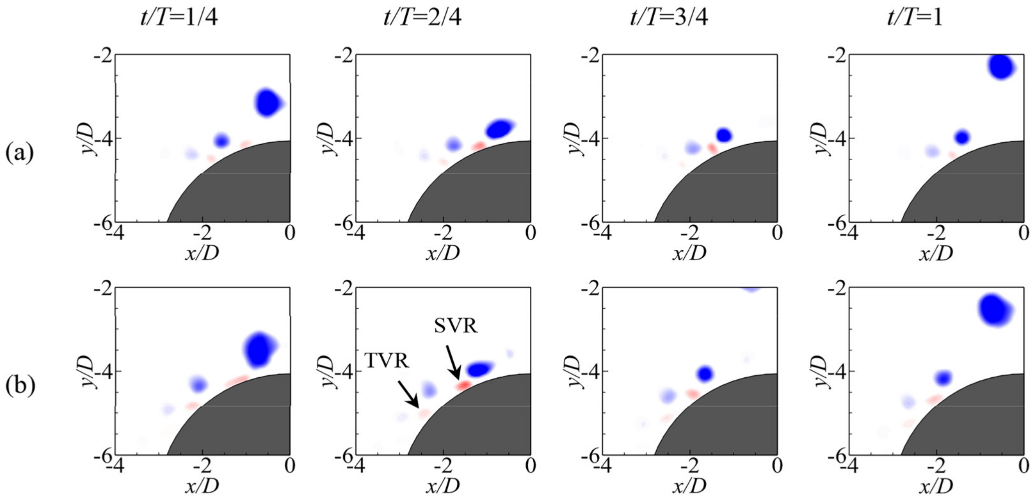

FIG. 6. Phase-averaged λ_{ci} fields of vortex ring impingement on a $d/D = 6$ sphere surface for all Reynolds numbers. (a) $\mathrm{Re}_{sj} = 227$ and (b) $\mathrm{Re}_{sj} = 682$.

B. Vortex ring trajectory and circulation

Trajectories of PVR, SVR, and TVR near the wall are presented in Fig. 8. We note that the SVR and TVR were named induced vortex rings in Fig. 8 because they were too small to distinguish, and a white dotted line was used to connect the spherical center and formation position of the induced vortex ring at $\mathrm{Re}_{sj} = 227$. It was found that for the case of $d/D = 1$ and 6, there was no significant difference in the formation position of the induced vortex ring, whereas for $d/D = 16$, the formation position was close to the jet centerline with the increase in Reynolds number. In Fig. 8(a), where the vortex ring trajectories associated with the $d/D = 1$ sphere are shown, the PVR gradually approached the jet centerline ($x/D = 0$) when it convected downstream. It was observed that the angle between the SVR and the jet centerline decreased as the Reynolds number increased. This was

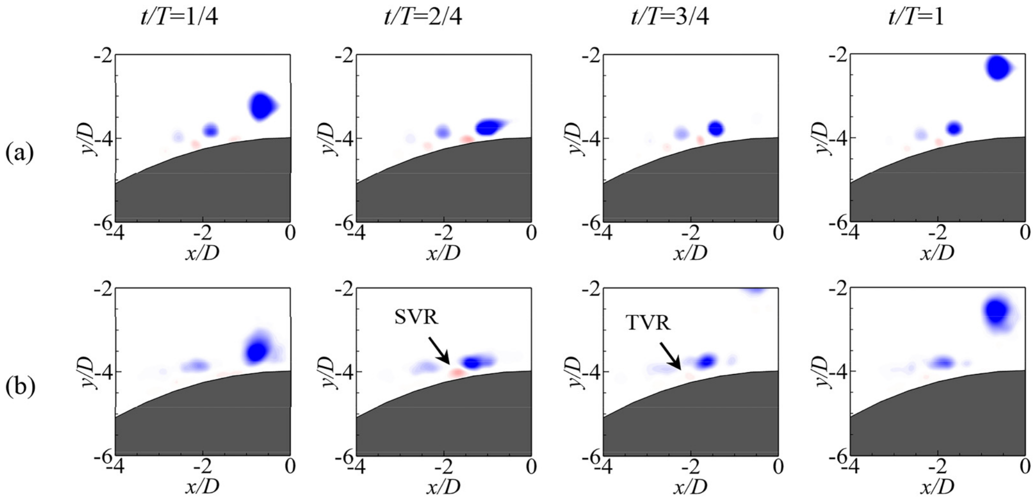

FIG. 7. Phase-averaged λ_{ci} fields of vortex ring impingement on a $d/D = 16$ sphere surface for all Reynolds numbers. (a) $\mathrm{Re}_{sj} = 227$ and (b) $\mathrm{Re}_{sj} = 682$.

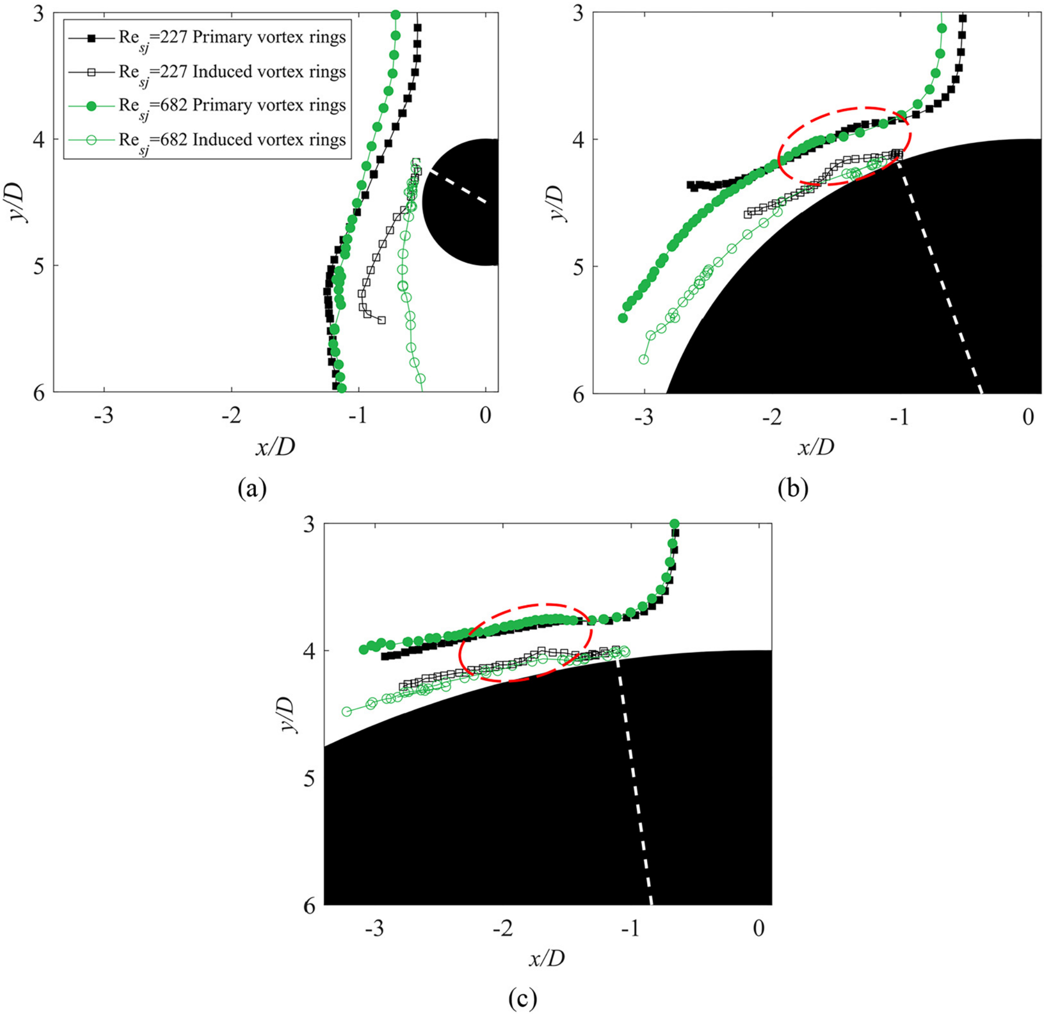

FIG. 8. Trajectories of the primary and induced vortex rings near the wall for all cases. (a) $d/D = 1$, (b) $d/D = 6$, and (c) $d/D = 16$.

because the PVR had a high strength to restrict the roll up of the SVR at a high Reynolds number. Additionally, the motion of the SVR was farther away due to the vortex ring strength increasing at a higher Reynolds number. Figure 8(b) shows the trajectories associated with the $d/D = 6$ sphere. The PVR and SVR expanded radially along the wall and then separated from the wall due to a mechanism similar to the inflectional instability" at $\mathrm{Re}_{sj} = 227$. However, when the Reynolds number was increased to 682, the primary and induced vortex rings expanded continuously along the wall until dissipation, and the expansion distances are longer than that at $\mathrm{Re}_{sj} = 227$. Finally, when the sphere diameter further increased to $d/D = 16$, the vortex rings expanded along the wall without separation. Obviously, the trajectory length of the PVR was shorter for a larger sphere, which showed that the PVR had a better expansion ability along the wall for a smaller diameter.

Interestingly, we observed that the vortex ring trajectories near the wall were wavy as marked by the red circle in Fig. 8. This phenomenon at a low Reynolds number can be attributed to the interaction between the primary and the induced vortex rings. The interaction process can be divided into four stages as presented in Figs. 9(a), 9(b), 9(c), and 9(d), respectively. In the first stage

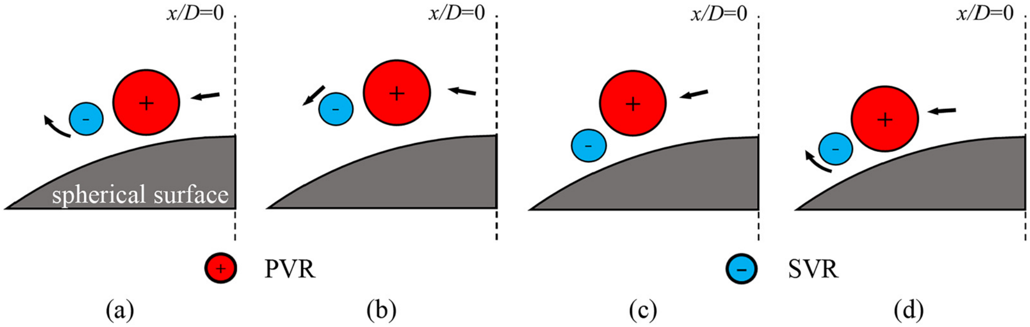

FIG. 9. Vortex ring behavior along the sphere surface, (a)–(d) correspond to stages 1–4 of vortex ring motion, respectively.

[Fig. 9(a)], the PVR induced and rolled up the SVR and then expanded along the wall. Subsequently, the interaction proceeded to the secondary stage [Fig. 9(b)]. The PVR had a tendency to separate from the wall due to the restriction and induction of the SVR. Meanwhile, the PVR motion caused the SVR to be close to the wall. In the third stage [Fig. 9(c)], the PVR was close to the wall under the influence of synthetic jets in the next cycle. Eventually, as the PVR approached, the SVR rolled up again [Fig. 9(d)]. However, when $\mathrm{Re}_{sj} = 682$, the SVR rolled up into the PVR in the secondary stage. Then, the TVR was induced and rolled up resulting in the induced vortex ring trajectories tilted up.

Additionally, we described trajectories of the PVR upstream for all cases in Fig. 10(a) to explore the effect of the Reynolds number and sphere diameter on the PVR incoming path. Obviously, the PVR incoming path width (i.e., vortex ring center position x_c) at a high Reynolds number is slightly larger than that at a low Reynolds number except $d/D = 16$. Furthermore, the PVR trajectories at $\mathrm{Re}_{sj} = 227, 682$ were extracted from Fig. 10 (a) and presented in Figs. 10(b) and 10(c), respectively. It was found that the PVR trajectory for $d/D = 16$ deviated from the incoming path for $d/D = 1$ and 6 at $\mathrm{Re}_{sj} = 227$, which may be explained by the interaction between the cluster structure and the PVR as shown in Fig. 4(a). For $d/D = 16$, the cluster structure formed and rotated, which interacted with the PVR resulting in trajectory deviation in $y/D > 2$. As the sphere diameter decreased to $d/D = 1$ and 6, the PVR had no effect on the PVR in the next cycle, and the incoming paths are basically consistent. The former can be attributed to the TVR convect downstream, whereas, the latter is because of the cluster structure being far away from the jet centerline. For the cases of all sphere diameters when $\mathrm{Re}_{sj} = 682$, the PVR expanded along the wall and cannot interact with the subsequent PVR, so the PVR incoming paths are basically consistent.

The vortex ring circulations are shown in Fig. 11 to shed light on the effects of Reynolds number and spherical diameter on the development of the primary and induced vortex rings by quantitative comparison. As depicted in Figs. 11(a) and 11(c), the circulation variations of the PVR had similar trends, which were divided into four stages for all tested cases. The first stage from $t/T = 0$ to 0.5, represented the formation of the PVR in which the circulation increased from zero to a peak rapidly. Subsequently, the vortex ring convected downstream in a stage of free development from $t/T = 0.5$ to approximately 1.1, within which circulation decreased gradually. The third stage denoted PVR impingement on the spherical wall. In this stage, circulation experienced its fastest decay due to the interaction between the vortex ring and wall. Finally, the PVR expanded along the wall. The residual circulation of vortex ring slowly reduced to zero because of viscous dissipation or a transition to turbulence. Furthermore, the circulation decreased more rapidly at a high Reynolds number, especially in the secondary and third stages due to weak stability and intense interaction, respectively, whereas no significant differences were observed for different spherical-diameter cases. These results showed that the Reynolds number had more influence on the development of the PVR compared to the sphere diameter. As shown in Figs. 11(b) and 11(d), the

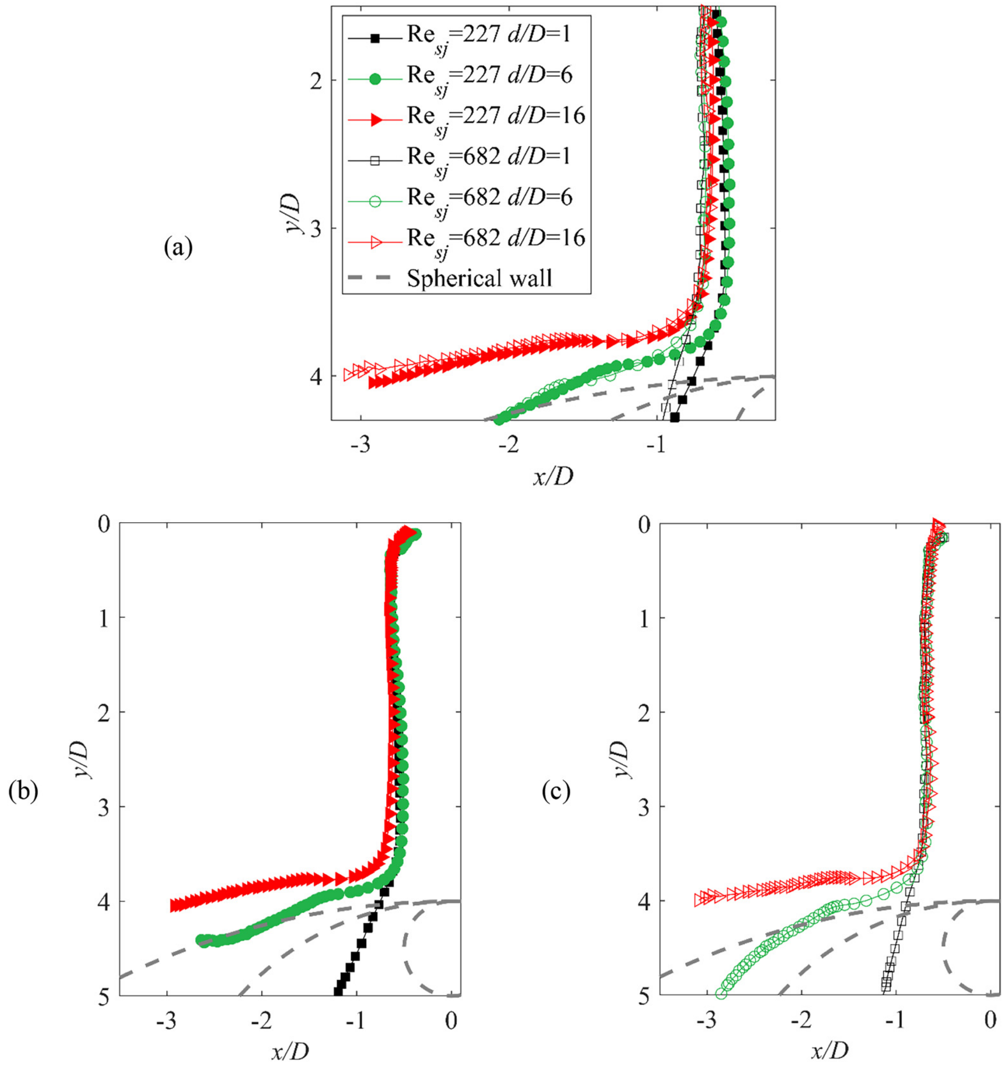

FIG. 10. Trajectories of the PVR upstream. (a) all cases, (b) $\mathrm{Re}_{sj} = 227$, and (c) $\mathrm{Re}_{sj} = 682$.

circulation of the induced vortex ring increased rapidly to its peak value and then decreased rapidly to zero for $d/D = 1$ at all tested Reynolds numbers. The former was caused by the formation of a SVR, whereas the latter was mainly because the SVR dissipated rapidly under the disturbance of the PVR after separation from the wall. For the cases of $d/D = 6$ and 16 when $\mathrm{Re}_{sj} = 227$, the circulation first experienced a fast decay and then decreased slowly to zero after the peak, which corresponded to the two stages of interaction with the PVR and dissipation due to viscosity. However, as the Reynolds number was increased to 682, the SVR dissipated rapidly after the first peak due to rolled into the PVR. Subsequently, because the TVR was induced at about $t/T = 1.7$ and 1.8 corresponding to the cases of $d/D = 6$ and 16, the circulation experienced a plateau or increased to a second peak. Finally, under the influence of fluid viscosity, circulation becomes so low that it cannot be measured. In particular, the circulation peaks of the induced vortex ring decreased with the increase in sphere diameter when the Reynolds number was kept constant, which indicated that when the vortex ring continues to expand, the wall curvature can drive the separation

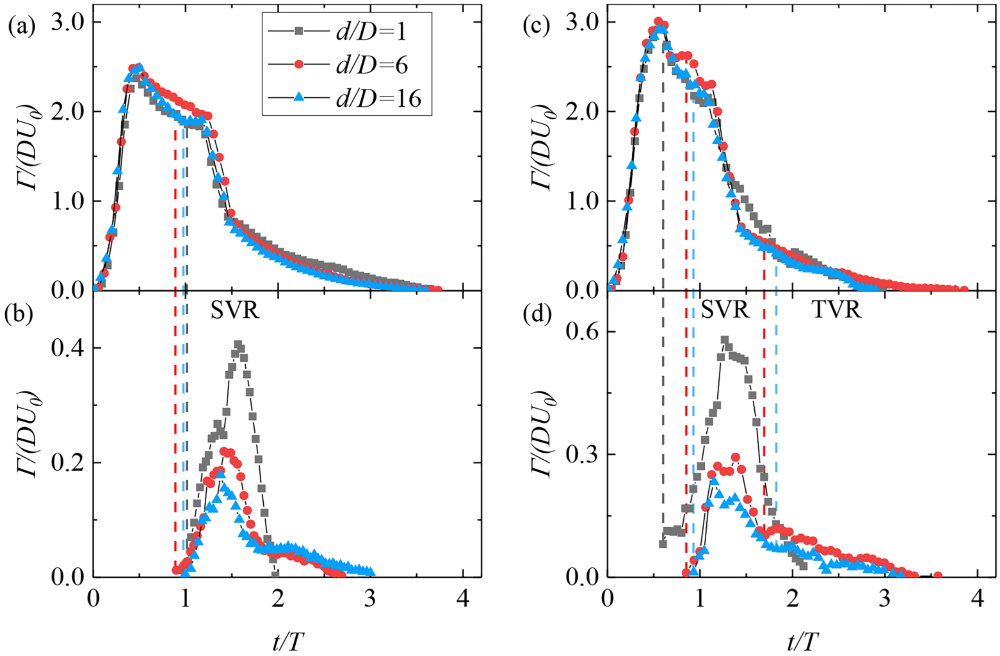

FIG. 11. Circulation variations of (a) PVR at $\mathrm{Re}_{sj} = 227$, (b) the induced vortex ring at $\mathrm{Re}_{sj} = 227$, (c) PVR at $\mathrm{Re}_{sj} = 682$, and (d) the induced vortex ring at $\mathrm{Re}_{sj} = 682$.

of the wall boundary layer and induces a SVR with high strength. This result may explain why the SVR-formation position was close to the jet centerline for large diameters at a high Reynolds number.

IV. CONCLUSION

Herein, the behavior of synthetic jet vortex rings impinging on a spherical surface was investigated for two parameters: sphere diameter and Reynolds number. The evolution of the vortex rings was analyzed by flow visualization and λ_{ci} fields. Furthermore, the vortex trajectories and circulation were calculated to reveal the influence of diameter and Reynolds number on the impingement process. The principal conclusions in the present experimental conditions are as follows.

It was found that the impingement flow was laminar at a low Reynolds number ($\mathrm{Re}_{sj} = 227$); therefore, the vortex ring losing coherence was attributed to the vorticity diffusion and viscous dissipation. In this case, a PVR with a low strength only induced a SVR. Meanwhile, a large-scale cluster structure formed at $d/D = 6$ and 16. For a sphere with a small diameter ($d/D = 1$), the PVR and SVR finally separated from the wall and convected downstream. As the diameter increased to $d/D = 6$, the vortex rings expanded at a certain distance on the upper sphere and then separated from the wall. As for the largest diameter ($d/D = 16$), the PVR and SVR expanded continuously along the wall without separation. As the Reynolds number was increased to 682, the PVR and SVR lost coherence rapidly when they convected downstream due to the vortex ring interaction being enhanced for the smallest diameter sphere ($d/D = 1$). For the cases of $d/D = 6$ and 16, the SVR was rolled up into the PVR. Subsequently, the PVR expanded along the wall continuously and induced a TVR. Finally, they lost coherence because of a transition to turbulence. This change in the impingement behavior at a high Reynolds number was because of the high-strength PVR.

The vortex ring trajectories illustrated that the sphere diameter can affect the vortex ring paths both on near wall and upstream. Specifically, the moving distance of the PVR decreased with the increase in sphere diameter. And the vortex ring trajectories near the wall like wavy because of the complex interaction between the PVR and the SVR for $d/D = 6$ and 16. Meanwhile, for the largest diameter ($d/D = 16$) at a low Reynolds number, the cluster structure close to the jet centerline can interact with the subsequent PVR and change the PVR incoming path. In addition, the sphere diameter had a significant effect on the strength of the SVR. The circulation results showed that under the drive of the curve, the separation of the wall boundary layer accelerated, and the circulation of the induced vortex ring increased with the decrease in sphere diameter.

ACKNOWLEDGMENTS

This experimental paper was financially supported by the National Natural Science Foundation of China (Grants No. U2106222, No. 52008140, and No. 51978222) and Heilongjiang Touyan Innovation Team Program.

[1] J. D. A. Walker, C. R. Smith, A. W. Cerra, and T. L. Doligalski, The impact of a vortex ring on a wall, J. Fluid Mech. **181**, 99 (1987).

[2] T. T. Lim, T. B. Nickels, and M. S. Chong, A note on the cause of rebound in the head-on collision of a vortex ring with a wall, Exp. Fluids **12**, 41 (1991).

[3] R. McKeown, R. Ostilla-Mónico, A. Pumir, M. P. Brenner, and S. M. Rubinstein, Emergence of small scales in vortex ring collisions, Phys. Rev. Fluids **3**, 100509 (2018).

[4] R. McKeown, R. Ostilla-Mónico, A. Pumir, M. P. Brenner, and S. M. Rubinstein, Cascade leading to the emergence of small structures in vortex ring collisions, Phys. Rev. Fluids **3**, 124702 (2018).

[5] P. Orlandi and R. Verzicco, Vortex rings impinging on walls: Axisyrnmetric and three-dimensional simulations, J. Fluid Mech. **256**, 615 (1993).

[6] J. D. Swearingen, J. D. Crouch, and R. A. Handler, Dynamics and stability of a vortex ring impacting a solid boundary, J. Fluid Mech. **297**, 1 (1995).

[7] C. C. Chu, C. T. Wang, and C. C. Chang, A vortex ring impinging on a solid plane surface-vortex structure and surface force, Phys. Fluids **7**, 1391 (1995).

[8] A. M. Naguib and M. M. Koochesfahani, On wall-pressure sources associated with the unsteady separation in a vortex-ring/wall interaction, Phys. Fluids **16**, 2613 (2004).

[9] M. Cheng, J. Lou, and L. S. Luo, Numerical study of a vortex ring impacting a flat wall, J. Fluid Mech. **660**, 430 (2010).

[10] T. T. Lim, An experimental study of a vortex ring interacting with an inclined wall, Exp. Fluids **7**, 453 (1989).

[11] T. H. New, S. Shi, and B. Zang, Some observations on vortex-ring collisions upon inclined surfaces, Exp. Fluids **57**, 109 (2016).

[12] T. H. New and B. Zang, Head-on collisions of vortex rings upon round cylinders, J. Fluid Mech. **833**, 648 (2017).

[13] C. Naaktgeboren, P. S. Krueger, and J. L. Lage, Interaction of a laminar vortex ring with a thin permeable screen, J. Fluid Mech. **707**, 260 (2012).

[14] D. Adhikari and T. T. Lim, The impact of a vortex ring on a porous screen, Fluid Dyn. Res. **41**, 051404 (2009).

[15] J. T. Hrynuk, J. Van Luipen, and D. Bohl, Flow visualization of a vortex ring interaction with porous surfaces, Phys. Fluids **24**, 037103 (2012).

[16] J. J. Allen, Y. Jouanne, and B. N. Shashikanth, Vortex interaction with a moving sphere, J. Fluid Mech. **587**, 337 (2007).

[17] P. J. S. A. Ferreira De Sousa, Three-dimensional instability on the interaction between a vortex and a stationary sphere, Theor. Comput. Fluid Dyn. **26**, 391 (2012).

[18] B. U. Felderhof, Coaxial collisions of a vortex ring and a sphere in an inviscid incompressible fluid, Phys. Fluids **29**, 043601 (2017).

[19] V. L. Nguyen, K. Takamure, and T. Uchiyama, Deformation of a vortex ring caused by its impingement on a sphere, Phys. Fluids **31**, 107108 (2019).

[20] J. C. Hu and S. D. Peterson, Vortex ring impingement on a wall with a coaxial aperture, Phys. Rev. Fluids **3**, 084701 (2018).

[21] A. Pavlova and M. Amitay, Electronic cooling using synthetic jet impingement, J. Heat Transfer **128**, 897 (2006).

[22] G. Krishnan and K. Mohseni, An experimental study of a radial wall jet formed by the normal impingement of a round synthetic jet, Eur. J. Mech. B/Fluids **29**, 269 (2010).

[23] Y. Xu and J. J. Wang, Flow structure evolution for laminar vortex rings impinging onto a fixed solid wall, Exp. Therm. Fluid Sci. **75**, 211 (2016).

[24] Y. Xu, G. S. He, V. Kulkarni, and J. J. Wang, Experimental investigation of influence of Reynolds number on synthetic jet vortex rings impinging onto a solid wall, Exp. Fluids **58**, 1 (2017).

[25] Y. Xu and J. J. Wang, Digital particle image velocimetry study on parameter influence on the behavior of impinging synthetic jets, Exp. Therm. Fluid Sci. **100**, 11 (2019).

[26] Y. Xu, J.-J. Wang, L.-H. Feng, G.-S. He, and Z.-Y. Wang, Laminar vortex rings impinging onto porous walls with a constant porosity, J. Fluid Mech. **837**, 729 (2018).

[27] Y. Xu, Z. Y. Li, J. J. Wang, and L. J. Yang, On the interaction between turbulent vortex rings of a synthetic jet and porous walls, Phys. Fluids **31**, 105112 (2019).

[28] Z. Y. Li, Y. Xu, L. H. Feng, and J. J. Wang, Synthetic jet vortex rings impinging onto a porous wall: Reynolds number effect, Int. J. Heat Mass Transf. **137**, 951 (2019).

[29] Z. Y. Li, Y. Xu, and J. J. Wang, Similarity parameter for synthetic jet vortex rings impinging onto porous walls, AIAA J. **58**, 722 (2020).

[30] B. L. Smith and A. Glezer, The formation and evolution of synthetic jets, Phys. Fluids **10**, 2281 (1998).

[31] J. Zhou, R. J. Adrian, S. Balachandar, and T. M. Kendall, Mechanisms for generating coherent packets of hairpin vortices in channel flow, J. Fluid Mech. **387**, 353 (1999).

[32] R. J. Adrian, K. T. Christensen, and Z.-C. Liu, Analysis and interpretation of instantaneous turbulent velocity fields, Exp. Fluids **29**, 275 (2000).

[33] L. H. Feng and J. J. Wang, Circular cylinder vortex-synchronization control with a synthetic jet positioned at the rear stagnation point, J. Fluid Mech. **662**, 232 (2010).

[34] M. Ester, H.-P. Kriegel, J. Sander, and X. Xu, A density-based algorithm for discovering clusters in large spatial databases with noise, in *Proceedings of the 2nd Intlernational Conference on Knowledge Discovery and Data Mining* (AAAI Press, Portland, Oregon, 1996), pp. 226–331.

[35] S. Oeltze-Jafra, J. R. Cebral, G. Janiga, and B. Preim, Cluster analysis of vortical flow in simulations of cerebral aneurysm hemodynamics, IEEE Trans. Vis. Comput. Graph. **22**, 757 (2016).

[36] M. Gharib, E. Rambod, and K. Shariff, A universal time scale for vortex ring formation, J. Fluid Mech. **360**, 121 (1998).

[37] S. Zhong, M. Jabbal, H. Tang, L. Garcillan, F. Guo, N. Wood, and C. Warsop, Towards the design of synthetic-jet actuators for full-scale flight conditions, Flow, Turbul. Combust. **78**, 283 (2007).